Long-term instability of the inner Solar system: numerical experiments

Nam H. Hoang, Federico Mogavero, Jacques Laskar

Monthly Notices of the ROYAL ASTRONOMICAL SOCIETY

MNRAS **514,** 1342–1350 (2022) https://doi.org/10.1093/mnras/stac1299
Advance Access publication 2022 May 11

Long-term instability of the inner Solar system: numerical experiments

Nam H. Hoang ,★ Federico Mogavero ★ and Jacques Laskar
IMCCE, CNRS UMR 8028, Observatoire de Paris, Université PSL, Sorbonne Université, 77 Avenue Denfert-Rochereau, F-75014 Paris, France

Accepted 2022 April 25. in original form 2022 April 5

ABSTRACT

Apart from being chaotic, the inner planets in the Solar system constitute an open system, as they are forced by the regular long-term motion of the outer ones. No integrals of motion can bound a priori the stochastic wanderings in their high-dimensional phase space. Still, the probability of a dynamical instability is remarkably low over the next 5 billion years, a time-scale 1000 times longer than the Lyapunov time. The dynamical half-life of Mercury has indeed been estimated recently at 40 billion years. By means of the computer algebra system TRIP, we consider a set of dynamical models resulting from truncation of the forced secular dynamics recently proposed for the inner planets at different degrees in eccentricities and inclinations. Through ensembles of 10^3–10^5 numerical integrations spanning 5–100 Gyr, we find that the Hamiltonian truncated at degree 4 practically does not allow any instability over 5 Gyr. The destabilization is mainly due to terms of degree 6. This surprising result suggests an analogy to the Fermi–Pasta–Ulam–Tsingou problem, in which tangency to Toda Hamiltonian explains the very long time-scale of thermalization, which Fermi unsuccessfully looked for.

Key words: chaos – instabilities – celestial mechanics – planets and satellites: dynamical evolution and stability – methods: numerical – methods: statistical.

1 INTRODUCTION

Even though the planet orbits in the inner Solar system (ISS) are chaotic with a Lyapunov time of about 5 million years (Laskar 1989, 1990; Sussman & Wisdom 1992; Mogavero & Laskar 2021), they are still statistically very stable over a time-scale that is a thousand times longer. The probability of a Mercury eccentricity higher than 0.7 over the next 5 billion years, for example, is about 1 per cent from direct integrations of the Solar system (Laskar & Gastineau 2009; Abbot et al. 2021). This percentage agrees with the statistics of a dynamical instability observed in secular models where the dynamics is averaged over the planet mean longitudes (Laskar 2008; Mogavero & Laskar 2021). The statistical stability of the ISS over the remaining lifetime of the Sun as a main sequence star is intriguing, if one considers that it represents an open system, as it is forced by the very regular motion of the outer planets (Laskar 1990; Mogavero & Laskar 2021). No exactly conserved quantities, such as the energy or angular momentum, can bound a priori the chaotic wanderings of the system in its high-dimensional phase space.

The disproportion between the Lyapunov time and the destabilization time-scale of the ISS has been addressed by Batygin, Morbidelli & Holman (2015), building on previous works by Lithwick & Wu (2011) and Boué, Laskar & Farago (2012). Boué et al. (2012) consider the first-order secular dynamics of a mass-less Mercury in the gravitational field of all the other planets, whose orbits are predetermined to a quasi-periodic form. They use a multipolar expansion of the Hamiltonian to show that very high Mercury eccentricities appear in the reduced phase space of the resonance $g_1 - g_5$ (involving the fundamental precession frequencies of the Mercury and Jupiter perihelia), which confirms the role of this harmonic in the destabilization of the ISS (Batygin & Laughlin 2008; Laskar 2008; Laskar & Gastineau 2009). Batygin et al. (2015) expand the secular Hamiltonian to degree 4 in eccentricities and inclinations of the planets, and study a few of its Fourier harmonics related to the fundamental frequencies g_1, g_2, g_5, s_1, and s_2. Their simplified dynamics is however much more unstable than realistic models, the typical time for the destabilization of Mercury orbit being around 1 Gyr (Woillez & Bouchet 2020). Recently, Mogavero & Laskar (2021, hereafter ML21) have proposed the model of a forced secular ISS, in which the outer planets only are frozen to quasi-periodic orbits. With a numerical experiment over 100 Gyr, they estimate the dynamical half-life of Mercury at 40 Gyr, consistently with the small probability of an instability over 5 Gyr.

Here we employ the computer algebra software TRIP (Gastineau & Laskar 2011, 2021) to perform truncation of the forced secular ISS at different degrees in eccentricities and inclinations. Through ensembles of 10^3–10^5 numerical integrations spanning 5–100 Gyr, we show how dynamical contributions usually deemed as unimportant, that is, high-degree terms of the Hamiltonian and non-resonant harmonics, strongly affect the probability of an instability over 5 Gyr.

2 DYNAMICAL MODELS

In the forced secular model of the ISS (detailed presentation in ML21), the orbits of the outer planets are predetermined to a quasi-periodic form, whose frequencies and amplitudes are inferred from frequency analysis (Laskar 1988, 2005) of a comprehensive model of the Solar system (Laskar et al. 2011). The secular gravitational interactions are considered at first order in planetary masses, which corresponds to Gauss' dynamics of Keplerian rings (Gauss 1818), and the leading contribution of general relativity (GR) is included.

★ E-mail: nam.hoang-hoai@obspm.fr (NH); federico.mogavero@obspm.fr (FM)

Table 1. Probability $P(\sup_{t\leq 5\,\mathrm{Gyr}} e_1(t) \geq e_{\max})$ in percent and its 90 per cent confidence interval, where e_1 is Mercury's eccentricity, for the dynamical models $\mathcal{H}_{2n}$, $\mathcal{H}$, $\mathcal{L}_{2n}$, and LG09.

$e_{\max}$	$\mathcal{H}_4$	$\mathcal{H}_6$	$\mathcal{H}_8$	$\mathcal{H}_{10}$	$\mathcal{H}$		$\mathcal{L}_4$	$\mathcal{L}_6$	LG09
0.35	$38.793^{39.037}_{38.549}$	$58.91^{59.16}_{58.66}$	$56.90^{57.68}_{56.11}$	$52.95^{53.74}_{52.16}$	$49.67^{50.47}_{48.87}$		$40.289^{40.558}_{40.020}$	$47.20^{47.44}_{46.96}$	$49.22^{51.54}_{46.90}$
0.4	$13.294^{13.464}_{13.124}$	$31.62^{31.85}_{31.39}$	$29.05^{29.77}_{28.33}$	$25.33^{26.03}_{24.65}$	$21.19^{21.85}_{20.55}$		$13.698^{13.887}_{13.510}$	$24.47^{24.67}_{24.26}$	$25.55^{27.63}_{23.58}$
0.5	$0.483^{0.519}_{0.450}$	$5.12^{5.24}_{5.02}$	$5.04^{5.39}_{4.70}$	$2.95^{3.23}_{2.70}$	$2.04^{2.27}_{1.82}$		$0.730^{0.778}_{0.685}$	$3.85^{3.94}_{3.76}$	$3.96^{4.97}_{3.15}$
0.6	$0.012^{0.019}_{0.008}$	$1.53^{1.59}_{1.47}$	$2.40^{2.65}_{2.17}$	$1.15^{1.33}_{0.99}$	$0.52^{0.65}_{0.42}$		$0.056^{0.070}_{0.044}$	$1.84^{1.90}_{1.77}$	$0.96^{1.53}_{0.60}$
0.7	$0.001^{0.004}_{0.000}$	$1.06^{1.11}_{1.01}$	$2.07^{2.31}_{1.86}$	$1.08^{1.26}_{0.93}$	$0.45^{0.57}_{0.35}$		$0.010^{0.017}_{0.006}$	$1.41^{1.47}_{1.36}$	$0.92^{1.48}_{0.57}$
0.8	$0.001^{0.004}_{0.000}$	$0.75^{0.79}_{0.71}$	$1.91^{2.14}_{1.70}$	$1.02^{1.19}_{0.87}$	$0.40^{0.57}_{0.28}$	$0.41^{0.52}_{0.32}$	$0.006^{0.011}_{0.003}$	$1.20^{1.25}_{1.15}$	$0.88^{1.43}_{0.54}$
0.9	$0.000^{0.003}_{0.000}$	$0.42^{0.45}_{0.38}$	$1.78^{2.00}_{1.58}$	$1.00^{1.17}_{0.85}$	$0.14^{0.26}_{0.08}$	$0.40^{0.51}_{0.31}$	$0.000^{0.003}_{0.000}$	$0.85^{0.89}_{0.80}$	$0.84^{1.38}_{0.51}$

Notes. LG09 represents the 2501 direct integrations of Laskar & Gastineau (2009). $\mathcal{H}$ denotes the 10 560 orbital solutions of Gauss' dynamics in ML21, and the two values of the last two rows of $\mathcal{H}$ correspond to the lower and upper bounds of the estimations, as explained in the text.

We remark that the shift of the frequency g_1 due to GR is comparable to the half-width of the principal secular resonances (Mogavero & Laskar 2022), and cannot be considered as a small correction.

With the aid of TRIP, the secular Hamiltonian $\widehat{H}$ of the entire Solar system, at first order in planetary masses, can be expanded in series of the complex Poincaré variables of the planets, i.e. $(x_i, \bar{x}_i, y_i, \bar{y}_i)_{i=1}^{8}$ (Laskar & Robutel 1995). The planets are indexed in order of increasing semi-major axis, as usual. Truncation at total degree $2n$ results in a polynomial Hamiltonian $\widehat{H}_{2n}$. When the predetermined orbits of the outer planets $(x_i(t), y_i(t))_{i=5}^{8}$ are substituted, one obtains the Hamiltonian of the forced ISS truncated at degree $2n$, i.e. $\mathcal{H}_{2n}((x_i, y_i)_{i=1}^{4}, t) = \widehat{H}_{2n}((x_i, y_i)_{i=1}^{4}, (x_i = x_i(t), y_i = y_i(t))_{i=5}^{8})$. The non truncated Hamiltonian, formally $\mathcal{H} = \mathcal{H}_\infty$, represents Gauss' dynamics of the forced ISS.

At the lowest degree, $\mathcal{H}_2$ describes an integrable forced Laplace–Lagrange dynamics. Its analytical solution can be obtained by a canonical transformation to the complex proper modes variables $(u_i, v_i)_{i=1}^{4}$, with corresponding action-angle variables $(X_i, \chi_i; \Psi_i, \psi_i)$ such that $(u_i = \sqrt{X_i}E^{-j\chi_i}; v_i = \sqrt{\Psi_i}E^{-j\psi_i})$.[1] When expressed in these action-angle variables, the truncated Hamiltonian is a finite Fourier series:

$$\mathbb{H}_{2n}(\boldsymbol{I}, \boldsymbol{\theta}, t) = \sum_{\boldsymbol{k},\boldsymbol{\ell}} \widetilde{\mathbb{H}}_{2n}^{\boldsymbol{k},\boldsymbol{\ell}}(\boldsymbol{I}) E^{j(\boldsymbol{k}\cdot\boldsymbol{\theta}+\boldsymbol{\ell}\cdot\boldsymbol{\omega}_o t)}, \quad \widetilde{\mathbb{H}}_{2n}^{\boldsymbol{k},\boldsymbol{\ell}} = \sum_{p=1}^{n} \widetilde{\mathbb{H}}_{(2p)}^{\boldsymbol{k},\boldsymbol{\ell}}, \tag{1}$$

where $\boldsymbol{I} = (\boldsymbol{X}, \boldsymbol{\Psi})$ and $\boldsymbol{\theta} = (\boldsymbol{\chi}, \boldsymbol{\psi})$ are the eight-dimensional vectors of the action and angle variables, respectively, t is the time, $\boldsymbol{\omega}_o = (g_5, g_6, g_7, g_8, s_6, s_7, s_8)$ is the septuple of the constant fundamental frequencies of the outer orbits (Laskar 1990), and $(\boldsymbol{k}, \boldsymbol{\ell}) \in \mathbb{Z}^8 \times \mathbb{Z}^7$ is the wave vector of a given harmonic. The amplitude of a harmonic $\widetilde{\mathbb{H}}_{2n}^{\boldsymbol{k},\boldsymbol{\ell}}$ consists of partial contributions $\widetilde{\mathbb{H}}_{(2p)}^{\boldsymbol{k},\boldsymbol{\ell}}$ from terms of the same degree $2p \leq 2n$. To identify these partial contributions, we define

$$\mathcal{F}_{(2p)}^{\boldsymbol{k},\boldsymbol{\ell}} = \widetilde{\mathbb{H}}_{(2p)}^{\boldsymbol{k},\boldsymbol{\ell}} E^{j(\boldsymbol{k}\cdot\boldsymbol{\theta}+\boldsymbol{\ell}\cdot\boldsymbol{\omega}_o t)} + c.c., \tag{2}$$

where c.c. refers to the complex conjugate. The order of a harmonic is defined as the even integer $\|(\boldsymbol{k}, \boldsymbol{\ell})\|_1 \leq 2n$, where $\|\cdot\|_1$ denotes the 1-norm. Since the quasi-periodic form of the outer orbits contains harmonics of order higher than one, the dynamics of $\mathcal{H}_{2n}$ and $\mathbb{H}_{2n}$ are not exactly the same. Yet, the difference is unimportant for the results of this work, so we shall treat the two Hamiltonians as equivalent from now on.

[1] E represents the exponential operator, j stands for the imaginary unit.

Second order in planetary masses

To investigate the effect of the order of the secular averaging on the long-term statistics, we employ the autonomous polynomial equations of motion of Laskar (1985, 1990) for the ensemble of the Solar system planets. These equations formally derive from a Hamiltonian of order two in masses and degree 6 in eccentricities and inclinations, and will be denoted as $\mathcal{L}_6$ throughout this paper. In this work, we also implement a variant of this dynamics, in which the equations for the inner planets are truncated at total degree 3 in eccentricities and inclinations, while those of the outer planets are kept at degree 5 (Appendix A). This new model, denoted as $\mathcal{L}_4$, is meant as an analogue of $\mathcal{H}_4$ at second order in masses.

3 NUMERICAL EXPERIMENTS

We systematically derive the equations of motion for the truncated Hamiltonians $\mathcal{H}_{2n}$ in TRIP. They are numerically integrated via an Adams PECE scheme of order 12, with a time-step of 250 yr. Typical integration times are given in ML21 (Table 1).

All the orbital solutions of $\mathcal{H}_{2n}$ in this paper correspond to initial conditions taken from a unique ensemble of 108 000 values very close to each other, and distributed according to

$$x_i = x_i^* + \sigma \left(\mathrm{Re}\{x_i^*\}\, z_i + j\, \mathrm{Im}\{x_i^*\}\, z_i' \right), \tag{3}$$

where x_i^* represents the nominal initial conditions for $\mathcal{H}$ given in ML21 (Appendix D), $z_i, z_i' \sim \mathcal{N}(0, 1)$ are standard normal deviates, and $\sigma = 10^{-9}$. An analogous expression holds for the variables (y_i). Initial conditions for (u_i, v_i) are directly derived from the transformation $(x_i, y_i) \rightarrow (u_i, v_i)$. For the first few million years, all the solutions reproduce the comprehensive direct simulation LaX13b (ML21), while they diverge from each other after about 100 Myr due to chaos. The choice of the initial distribution has an impact on the secular solutions that decreases with time because of chaotic diffusion (Hoang, Mogavero & Laskar 2021). Therefore, the long-term statistics we present should not depend on its particular shape, but should rather reflect the nature of the dynamical models employed.

We compute 108 000 solutions spanning 5 Gyr in the future for $\mathcal{H}_4$ and $\mathcal{H}_6$, and 10 800 solutions for $\mathcal{H}_8$ and $\mathcal{H}_{10}$ over the same time interval. For each Hamiltonian, we prolong 1 080 solutions to 100 Gyr. The statistics of $\mathcal{L}_6$ was first described in (Laskar 2008) with 478 solutions integrated up to 5 Gyr. In this paper, we compute a much larger ensemble of solutions: 120 000 and 40 000 solutions at degree 6 lasting for 5 and 100 Gyr in the future, respectively; 90 000 and 10 000 solutions at degree 4 ($\mathcal{L}_4$) spanning the same

intervals. The statistics of this paper will be compared with those from previous works: the forced secular ISS without truncation in eccentricities nor in inclinations, i.e. Gauss' dynamics, denoted as $\mathcal{H}$ (ML21); the direct integrations of the Solar system of Laskar & Gastineau (2009, hereafter LG09).

For each ensemble of solutions, we retrieve the statistics of the maximum value reached by the eccentricity of Mercury over a given time-span (Laskar 1994) This choice is motivated by the fact that the excitation of Mercury's eccentricity due to the resonance $g_1 - g_5$ is a precursor of the dynamical instability. Mercury's eccentricity at 5 Gyr typically ranges from 0 and 0.5 (Laskar 2008; LG09; ML21). The rare activation of the resonance $g_1 - g_5$ allows a net transfer of angular momentum deficit (Laskar 1997) from the outer planets to the ISS, and pump the eccentricity of Mercury to a higher value. Once the eccentricity of Mercury exceeds 0.7, the solutions enter an unstable regime, where close encounters and collisions involving Mercury become possible. Therefore, a Mercury's eccentricity higher than 0.7 shall be taken as a synonym of instability for the rest of the paper.

All the secular solutions are stopped at numerical instability, except those of Gauss' dynamics that end at a secular collision, that is, the geometric intersection of the Keplerian ellipses of two planets (ML21). To have a more accurate comparison, we assume that after a secular collision, the maximum Mercury eccentricity of a Gauss' solution exceeds 0.9 shortly, which corresponds to the upper bounds of the column $\mathcal{H}$ in Table 1. This assumption for the solutions of $\mathcal{H}$ is used for the remainder of this paper. In contrast, the lower bounds assume that the maximum eccentricity of Mercury of such solutions does not reach higher values after a secular collision, and correspond to the statistics reported in ML21 (Table 4).

4 STATISTICS OF MERCURY'S ECCENTRICITY

4.1 Small changes, big differences over 5 Gyr

Table 1 shows for each dynamical model the percentages of solutions whose Mercury's maximum eccentricity over 5 Gyr reaches various values, from 0.35 to 0.9. We report statistical confidence bounds estimated by Wilson's (1927) score interval at 90 per cent level. A temporal evolution of the statistics is presented in Fig. 1, which displays the cumulative distribution functions (CDFs) of $\tau = \inf_t\{e_1(t) \geq 0.7\}$, that is, the first time that the eccentricity of Mercury e_1 reaches the threshold of 0.7 along a given solution (the variation of the CDFs with different thresholds is studied in Appendix B). The values of the curves at 5 Gyr coincide with the line of 0.7 of Table 1.

The most striking results from Fig. 1 and Table 1 lie in the statistics of the models of degree 4, $\mathcal{H}_4$ and $\mathcal{L}_4$. The probability of a high Mercury eccentricity over 5 Gyr is around 1 per cent in LG09, which is considered as the reference model, and this is reproduced up to a factor of two by all the models of degree 6 and higher. Nevertheless, the dynamics of $\mathcal{H}_4$ is much more stable, with only one solution among 108 000 in which Mercury's eccentricity exceeds 0.7, for an estimated probability of 10^{-5}, a thousand times smaller than that of the reference model. At second order in planetary masses, the disparity between $\mathcal{L}_4$ and $\mathcal{L}_6$ is two orders of magnitude, which is still substantial. The CDF of $\mathcal{L}_6$ is slightly greater than that of $\mathcal{H}_6$, which shows that the contribution of the second order in planetary masses is small and destabilizing. Nevertheless, for such a stable model like $\mathcal{H}_4$, the second order can still raise the instability rate by one order of magnitude.

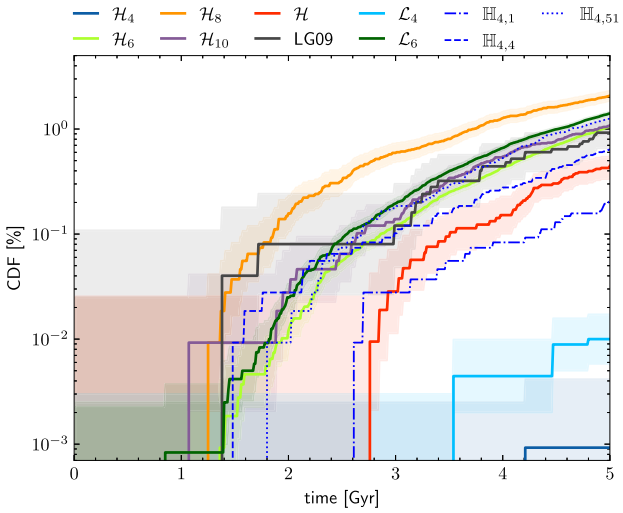

Figure 1. CDF of the first hitting time of Mercury's eccentricity at 0.7 over 5 Gyr with 90 per cent piecewise confidence interval, for the dynamics $\mathcal{H}_{2n}$, $\mathbb{H}_{4,m}$, $\mathcal{H}$, $\mathcal{L}_{2n}$, and LG09. LG09 represents 2492 direct integrations[2](LG09), $\mathcal{H}$ denotes 10 560 solutions of Gauss' dynamics (ML21).

The great stability of the $\mathcal{H}_4$ dynamics shows that the low probability of 1 per cent for an instability of Mercury orbit over 5 Gyr should be interpreted as a perturbative effect, with the leading contribution coming from the Hamiltonian terms of degree 6. The practical stability of $\mathcal{H}_4$ over 5 Gyr is unexpected, since it still reproduces the chaotic dynamics of the ISS with the same long-term statistical distribution of the maximum Lyapunov exponent as in $\mathcal{H}_6$ or Gauss' dynamics (Mogavero & Laskar 2022). It also shows the same destabilization mechanism, that is, the activation of the resonance $g_1 - g_5$. Previous works on the instability of Mercury orbit studied a simplified dynamics in which only a few Fourier harmonics of $\mathcal{H}_4$ are considered (Batygin et al. 2015; Woillez & Bouchet 2020). This latter model is actually considerably more unstable than the reference model LG09, in deep contrast with the practical stable dynamics of $\mathcal{H}_4$ over 5 Gyr.

The secular models of degree higher than 4 give predictions that generally agree with the N-body integrations LG09. While Gauss's dynamics tends to underestimate, and $\mathcal{H}_8$ overestimates the instability probability, $\mathcal{H}_{10}$ gives accurate predictions (this is probably a coincidence related to the behaviour of the series expansion). At times shorter than 5 Gyr and for a threshold of 0.7, the estimations of $\mathcal{H}_6$, $\mathcal{H}_{10}$, and $\mathcal{L}_6$ generally agrees with the results of a refined method of rare event detection applied to direct integrations (Abbot et al. 2021)[3]: For $\mathcal{L}_6$, the probability of Mercury orbit having eccentricity larger than 0.7 in the next 2 Gyr is 0.025 per cent with a 90 per cent confidence interval (0.019 per cent, 0.034 per cent), while it is 0.2 per cent with a 90 per cent confidence interval (0.18 per cent, 0.22 per cent) over 3 Gyr. The Hamiltonians of degree 4 and 6 show a relatively pronounced decay of the probability from 0.7 to 0.9 (see also Fig. B1). This interesting phenomenon is inherent to degree 6 or lower, because the probability of the models of higher

[2]9 out of the original 2501 solutions were damaged during data storage.

[3]The definition of instability in Abbot et al. (2021) is however different.

degree is fairly constant across high values of Mercury's eccentricity: If e_1 reaches 0.7 along a solution, it also probably goes beyond 0.9.

4.2 Ranking of harmonics according to their contributions to g_1

In order to explain the difference between the statistics of $\mathcal{H}_4$ and $\mathcal{H}_6$, we shall switch to the proper mode variables and the Fourier representation of equation (1). The Hamiltonian $\mathbb{H}_6$ contains substantially more harmonics than $\mathbb{H}_4$, 69 339 compared to 2748. For each harmonic of $\mathbb{H}_4$, $\mathbb{H}_6$ includes additional terms of degree 6 in its amplitude. Despite the large difference in the number of terms, most of the contributions of $\mathbb{H}_6$ are negligible. We aim to identify here the Fourier harmonics that have an important impact on the destabilization mechanism, that is, the activation of the resonance $g_1 - g_5$. Because g_5 is constant in the forced dynamics, we shall focus on the fundamental precession frequency of Mercury perihelion g_1.

Following ML21, the instantaneous value of the frequency g_1 for the Hamiltonian $\mathbb{H}_{2n}$ is defined as

$$\hat{g}_1^{(2n)} = -\dot{\theta}_1 = -\frac{\partial \mathbb{H}_{2n}}{\partial I_1} = \sum_{\boldsymbol{k},\boldsymbol{\ell}} \sum_{p=1}^{n} \hat{g}_{1(2p)}^{\boldsymbol{k},\boldsymbol{\ell}}, \tag{4}$$

where the partial contribution at degree $2p$ of each harmonic is

$$\hat{g}_{1(2p)}^{\boldsymbol{k},\boldsymbol{\ell}} = -\frac{\partial \mathcal{F}_{(2p)}^{\boldsymbol{k},\boldsymbol{\ell}}(\boldsymbol{I})}{\partial I_1} = -\frac{\partial \widetilde{\mathbb{H}}_{(2p)}^{\boldsymbol{k},\boldsymbol{\ell}}(\boldsymbol{I})}{\partial I_1} E^{j(\boldsymbol{k}\cdot\boldsymbol{\theta}+\boldsymbol{\ell}\cdot\boldsymbol{\omega}_o t)} + c.c.. \tag{5}$$

In this form, each harmonic manifests its importance via its direct contribution to g_1, which varies along an orbital solution according to the position in the phase space, i.e. $\hat{g}_{1(2p)}^{\boldsymbol{k},\boldsymbol{\ell}}(t) = \hat{g}_{1(2p)}^{\boldsymbol{k},\boldsymbol{\ell}}(\boldsymbol{I}(t), \boldsymbol{\theta}(t), t)$. To identify the main harmonics involved in the destabilization of the dynamics, equations (4) and (5) are evaluated along unstable solutions. Short-term oscillations are suppressed by the low-pass Kolmogorov–Zurbenko (KZ) filter (Yang & Zurbenko 2010), which is applied to the instantaneous frequency g_1 and its harmonic contributions. We use the KZ filter with three iterations of the moving average and a cut-off frequency of (1 Myr)$^{-1}$ (ML21, Appendix B) to obtain the filtered values

$$g_1^{(2n)} = \mathrm{KZ}(\hat{g}_1^{(2n)}), \quad g_{1(2p)}^{\boldsymbol{k},\boldsymbol{\ell}} = \mathrm{KZ}(\hat{g}_{1(2p)}^{\boldsymbol{k},\boldsymbol{\ell}}). \tag{6}$$

The harmonics can then be ranked according to the maximum value of their absolute filtered contribution over the time interval $[0, T]$. The time-span T is chosen to be slightly larger than the time of the first activation[4] of the resonance $g_1 - g_5$. After this point, the system either exhibits a secular collision right away or enters a period of excited dynamics before an eventual collision. This unstable state typically lasts longer for a solution of $\mathcal{H}_6$ than for a Hamiltonian of higher degree.

We establish the harmonic ranking on an unstable solution of $\mathcal{H}_6$, whose Mercury's eccentricity over time is shown in Fig. 2 (the ranking of the leading harmonics is quite robust when we switch to other unstable solutions). The first entrance into the chaotic zone of the resonance $g_1 - g_5$ occurs just after 1.97 Gyr (see Fig. 3a), during which the eccentricity of Mercury is pumped to 0.65 and the harmonic contributions generally reach their maximum values (see Fig. 3b). The ranking is computed over the first 2 Gyr to capture the contributions of the harmonics at the resonance. Table 2 shows two harmonic rankings based on the partial contributions at degree 4 and 6, respectively. It is surprising to find that the contributions to g_1 at degree 6 are slightly less, but still roughly the same amount as those at degree 4. Because the principal contributions at degree 6 come from harmonics of order 2 and 4, what $\mathbb{H}_6$ mainly offers is not new resonances, but rather corrections to the existing harmonics of $\mathbb{H}_4$. The corrections at degree 6 help to push g_1 toward g_5 and bring the solution closer to the destabilizing resonance. Geometrically speaking, in the phase space the resonance $g_1 - g_5$ defined by $\mathbb{H}_6$ is closer to the current ISS than that of $\mathbb{H}_4$.

[4]Throughout the paper, by *activation* we mean the exploration of the chaotic zone of the resonance, independently of the entrance in a libration state.

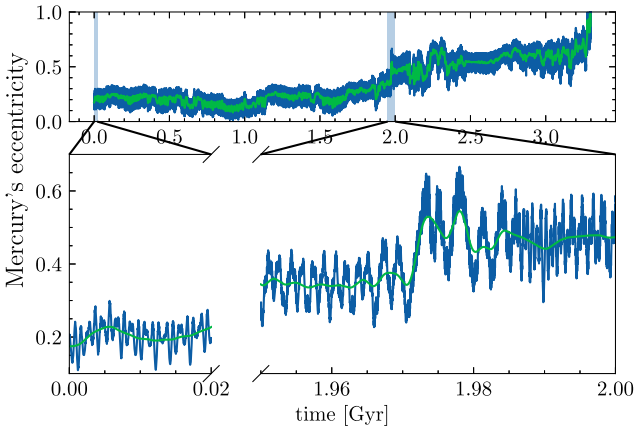

Figure 2. Temporal evolution of Mercury's eccentricity for an unstable solution of $\mathcal{H}_6$ (blue curve) and its KZ-filtered value with three iterations of the moving average and a cut-off frequency of (5 Myr)$^{-1}$ (green curve). The initial period of 20 Myr and the period of the first activation of the resonance $g_1 - g_5$ from 1.95 to 2 Gyr are enlarged in the lower panel.

Fig. 3(b) gives a closer look at the time evolution of the leading harmonic contributions to g_1 at degree 6. They are small at the beginning when the solution is stable, but get much bigger when the eccentricity of Mercury becomes higher, that is during and after the first activation of the resonance $g_1 - g_5$ at 1.97 Gyr. During this period, which is shown in the lower panel of Fig. 3(b), the strongest terms are the null-frequency harmonic, i.e. the integrable part of the Hamiltonian $\widetilde{\mathbb{H}}_{(6)}^{\boldsymbol{0},\boldsymbol{0}}$, and the harmonic $s_1 - s_2$, which also enters resonance. These two terms tend to destabilize the system by decreasing g_1 by substantial amounts, which are even greater than the leading GR correction of 0.4 arcsec yr^{-1} at degree 2 at some point. In the opposite direction, the two harmonics $2g_1 - (s_1 + s_2)$ and $2(g_1 - s_1)$ raise g_1, moving it away from g_5. Although these terms are non resonant, they are extremely crucial for the stability of Mercury orbit (see Section 4.3). Other harmonics also contribute to g_1 at degree 6 in an alternating pattern, but to a lesser extent.

To confirm the crucial role of the terms of degree 6, we add them to $\mathbb{H}_4$ to construct partial Hamiltonians (Mogavero & Laskar 2022):

$$\mathbb{H}_{4,m} = \mathbb{H}_4 + \sum_{i=1}^{m} \mathcal{F}_{(6)}^{i}, \tag{7}$$

where $\mathcal{F}_{(6)}^{i} = \mathcal{F}_{(6)}^{\boldsymbol{k}_i,\boldsymbol{\ell}_i}$ is the ith harmonic from the ranking at degree 6 of Table 2, and m is the total number of such harmonics that are considered. Fig. 3(a) shows the filtered g_1 computed from different Hamiltonians along the same unstable trajectory of $\mathcal{H}_6$ of Fig. 2. Initially, when the solution is stable and Mercury's eccentricity is relatively low, the frequency $g_1^{(4)}$ of $\mathbb{H}_4$ is almost indistinguishable from the corresponding $g_1^{(6)}$ of $\mathbb{H}_6$. Across the activation of the resonance $g_1 - g_5$, the difference between the two frequencies becomes considerable: $g_1^{(6)}$ almost reaches g_5, while $g_1^{(4)}$ does not.

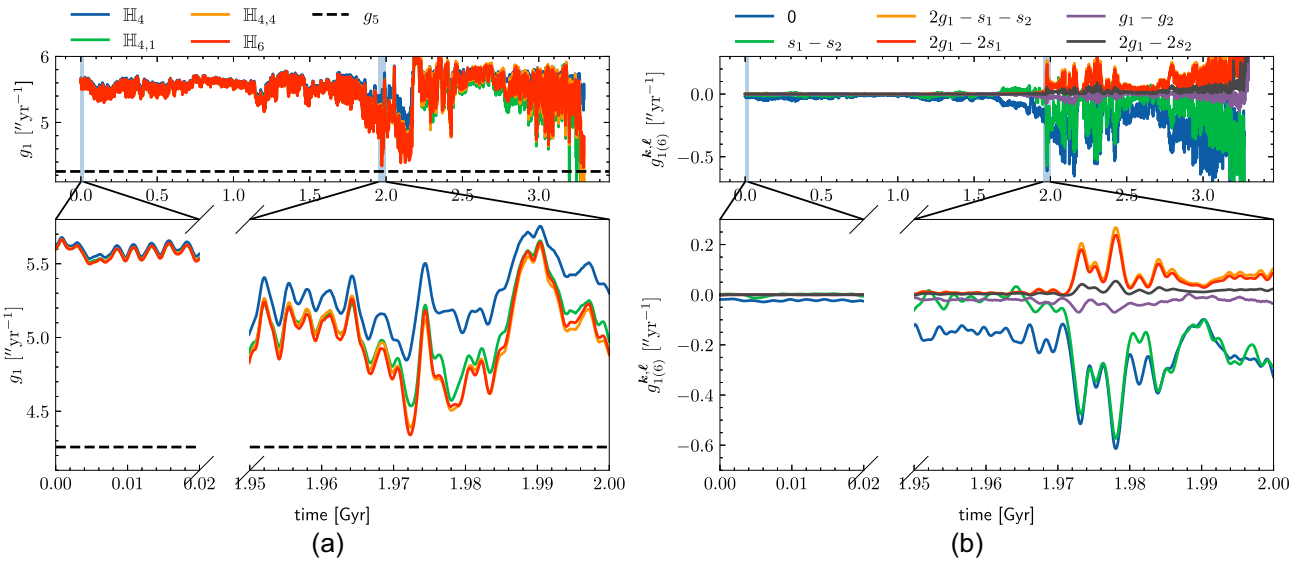

Figure 3. Temporal evolution of the filtered frequency g_1 defined from different Hamiltonians (left-hand panel) and partial contributions $g^{k,\ell}_{1(6)}$ at degree 6 from the six leading harmonics of Table 2 (right-hand panel) along the unstable integration of $\mathcal{H}_6$ of Fig. 2. The low-pass filter has a cut-off frequency of (1 Myr)$^{-1}$. The initial period of 20 Myr and the period of the first activation of the resonance $g_1 - g_5$ from 1.95 to 2 Gyr are enlarged in the lower panels.

Table 2. Rankings of Fourier harmonics.

i	Harmonic $\mathcal{F}^i_{(4)}$	$\mathcal{C}^{k,\ell}_{(4)}$	Harmonic $\mathcal{F}^i_{(6)}$	$\mathcal{C}^{k,\ell}_{(6)}$
1	0	−0.836	0	−0.614
2	$s_1 - s_2$	−0.790	$s_1 - s_2$	−0.573
3	$2g_1 - s_1 - s_2$	0.413	$2g_1 - s_1 - s_2$	0.268
4	$2g_1 - 2s_1$	0.366	$2g_1 - 2s_1$	0.237
5	$g_1 - g_5$	−0.126	$g_1 - g_2$	−0.071
6	$2g_1 - 2s_2$	0.117	$2g_1 - 2s_2$	0.054
7	$g_1 - g_2 + s_1 - s_2$	−0.054	$g_1 - g_5$	−0.053
8	$g_1 - g_2$	0.035	$g_1 - g_2 + s_1 - s_2$	−0.044
9	$g_1 - g_2 - s_1 + s_2$	−0.027	$2s_1 - 2s_2$	0.044
10	$s_1 - s_3$	0.024	$g_1 - g_2 - s_1 + s_2$	−0.039

Notes. Partial contributions to g_1 (arcsec yr^{-1}) from the harmonics at degree 4 ($\mathcal{F}^i_{(4)}$) and 6 ($\mathcal{F}^i_{(6)}$), along the unstable solution of $\mathcal{H}_6$ of Fig. 2. The maximum filtered contributions are denoted by $\mathcal{C}^{k,\ell}_{(2p)} = g^{k,\ell}_{1(2p)}(t^\star)$, with $t^\star = \arg\max_{t \le T} |g^{k,\ell}_{1(2p)}(t)|$(equations 5 and 6). For each partial degree, the harmonics are ranked according to $|\mathcal{C}^{k,\ell}_{(2p)}|$ with $T = 2$ Gyr, which is shortly after the first activation of the resonance $g_1 - g_5$.

The difference is mainly due to the integrable term $\widetilde{\mathbb{H}}^{\mathbf{0},\mathbf{0}}_{(6)}$, which is included in $\mathbb{H}_{4,1}$, and to the first leading harmonics contained in $\mathbb{H}_{4,4}$.

The statistics of the high Mercury eccentricities from $\mathbb{H}_{4,m}$ should approximate that of $\mathbb{H}_6$ better than $\mathbb{H}_4$. In order to test this expectation, we integrate the dynamics of $\mathbb{H}_{4,1}$, $\mathbb{H}_{4,4}$, and $\mathbb{H}_{4,51}$ from 10 800 and 1 080 initial conditions over 5 and 100 Gyr, respectively. The initial conditions are taken from the same ensembles employed for $\mathcal{H}_{2n}$. The CDFs of the first time that Mercury eccentricity reaches 0.7 for $\mathbb{H}_{4,m}$ are shown in Fig. 1. The wide discrepancy between $\mathcal{H}_4$ and $\mathcal{H}_6$ is first bridged by adding the integrable term $\widetilde{\mathbb{H}}^{\mathbf{0},\mathbf{0}}_{(6)}$, with which the curve of $\mathbb{H}_{4,1}$ attains a probability of 0.2 per cent at 5 Gyr. Including the next three leading harmonics brings the curve to the same level as Gauss' dynamics. Adding additional terms makes the statistics oscillate around that of $\mathbb{H}_6$.

The impact of the choice of the initial conditions on the present analysis deserves a discussion. As stated in Section 3, the nominal initial conditions of the truncated forced dynamics $\mathcal{H}_{2n}$ are chosen to be the same as those of Gauss' dynamics $\mathcal{H}$. In principle, they should be adapted to each model according to the harmonics that are dropped from the full Hamiltonian (Laskar & Simon 1988; ML21). Nevertheless, the lack of adjustment of the nominal initial conditions has a negligible effect in our study. First of all, the harmonic contributions to g_1 in Table 2 are established on an orbital solution of $\mathcal{H}_6$: The change in the initial conditions with respect to $\mathcal{H}$ is of only degree 8 in eccentricities and inclinations of the planets (Morbidelli 2002). Secondly, $\mathcal{H}_4$ and all the partial Hamiltonians considered in equation (7) contain the entire contribution from terms of degree 4. Therefore, the change in the initial conditions is still of degree 6. These considerations indicate that all the models considered here reproduce consistently the dynamics of the ISS on short (secular) time-scales, as shown for the frequency g_1 in the lower panel of Fig. 3(a). Moreover, the impact on long-term statistics of small differences among ensembles of initial conditions generally decreases with time because of chaotic diffusion (Hoang et al. 2021). As a result, our findings should not be sensitive to the initial displacement in the phase space, but rather reflect the distinctive long-term behaviour of the different models.

4.3 Importance of non-resonant harmonics

We have shown the importance of harmonics at degree 6 by adding them to $\mathbb{H}_4$ to construct partial Hamiltonians. Among the leading terms, there are several non-resonant harmonics, which are often considered unimportant when constructing simplified models. Among the leading non-resonant harmonics of Table 2, we consider $2g_1 - (s_1 + s_2)$, $2(g_1 - s_1)$, and $2(g_1 - s_2)$, to highlight their role in stabilizing the ISS. We shall subtract the entire contribution of these three harmonics from the Hamiltonians $\mathbb{H}_4$ and $\mathbb{H}_{4,m}$, to define new partial Hamiltonians denoted as $\mathbb{H}^*_4$ and $\mathbb{H}^*_{4,m}$, respectively. The values of m are chosen to be the same as in Section 4.2, that is, $m \in \{1, 4, 51\}$. We integrate the equations of motion defined by $\mathbb{H}^*_4$ and $\mathbb{H}^*_{4,m}$ over 5 Gyr from the same ensemble of initial conditions defined in Section 3, to obtain 10 800 solutions.

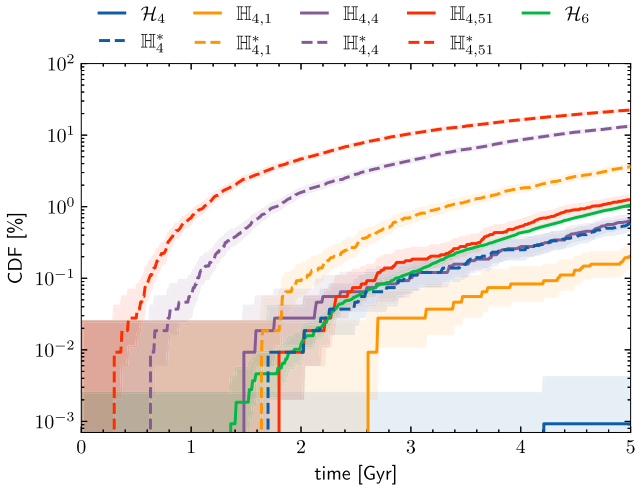

Figure 4. CDFs of the first hitting time of Mercury's eccentricity at 0.7 over 5 Gyr for the dynamical models $\mathcal{H}_4$, $\mathcal{H}_6$, $\mathbb{H}_{4,m}$ (solid lines), and $\mathbb{H}^*_4$, $\mathbb{H}^*_{4,m}$ (dashed lines). The Hamiltonians $\mathbb{H}^*_4$ and $\mathbb{H}^*_{4,m}$ exclude from $\mathbb{H}_4$ and $\mathbb{H}_{4,m}$, respectively, the entire contribution of the three non-resonant harmonics $2g_1 - (s_1 + s_2)$, $2(g_1 - s_1)$, and $2(g_1 - s_2)$ of Table 2.

Fig. 4 shows the comparison between $\mathbb{H}_4$, $\mathbb{H}_{4,m}$, and $\mathbb{H}^*_4$, $\mathbb{H}^*_{4,m}$ for the CDF of the first time that Mercury's eccentricity reaches 0.7 over 5 Gyr. For all the models, removing the three non-resonant harmonics makes the dynamics significantly more unstable, with at least one order of magnitude of difference. For comparison, the dynamics of $\mathcal{H}_4$ is a thousand times more stable than $\mathcal{H}_6$ over 5 Gyr, but taking away the three harmonics brings the model $\mathbb{H}^*_4$ basically to the same level of instability of $\mathcal{H}_6$. If we consider the Hamiltonian $\mathbb{H}^*_{4,51}$, based on $\mathbb{H}_{4,51}$ that is the closest dynamics to $\mathcal{H}_6$ among the presented partial Hamiltonians, its probability of instability is around 20 per cent at 5 Gyr, that is, twenty times more than the instability rate of $\mathcal{H}_6$. These numerical experiments show the crucial role of these non-resonant harmonics in stabilizing the ISS. Interestingly enough, all the three harmonics permits the exchange of angular momentum deficit between the eccentricity and inclination degrees of freedom, that is, between the proper modes (u_i) and (v_i). These results also show the sensitivity of the destabilization probability to the details of the dynamics, and may explain, at least partially, the great instability shown by the simplified models considered in literature (Batygin et al. 2015; Woillez & Bouchet 2020).

4.4 Statistics over 100 Gyr

To explore the dynamics in a regime where highly excited orbits no longer represent rare events, we follow ML21 and prolong 1080 integrations of the different Hamiltonians previously considered to 100 Gyr. Fig. 5 shows the CDFs of the first time that Mercury eccentricity reaches 0.7 and the corresponding probability density functions (PDFs). The PDFs are estimated by the debiased kernel density estimation (KDE) method (Cheng & Chen 2019), with Gaussian kernel and Silverman (1986)'s rule-of-thumb bandwidth (Appendix D). We use the log transformation and the pseudo-data method (Cowling & Hall 1996) to remove the boundary effects induced by the KDE at 0 and 100 Gyr, respectively. The confidence intervals of the PDFs are estimated by bootstrap (Efron 1979) of the debiased KDEs; for the CDFs, we use Wilson's score interval.

The CDFs of $\mathcal{H}_6$ and $\mathcal{H}_8$ are close to each other, with medians of 30 Gyr, while that of $\mathcal{H}_{10}$ is around 35 Gyr. The increasing values of

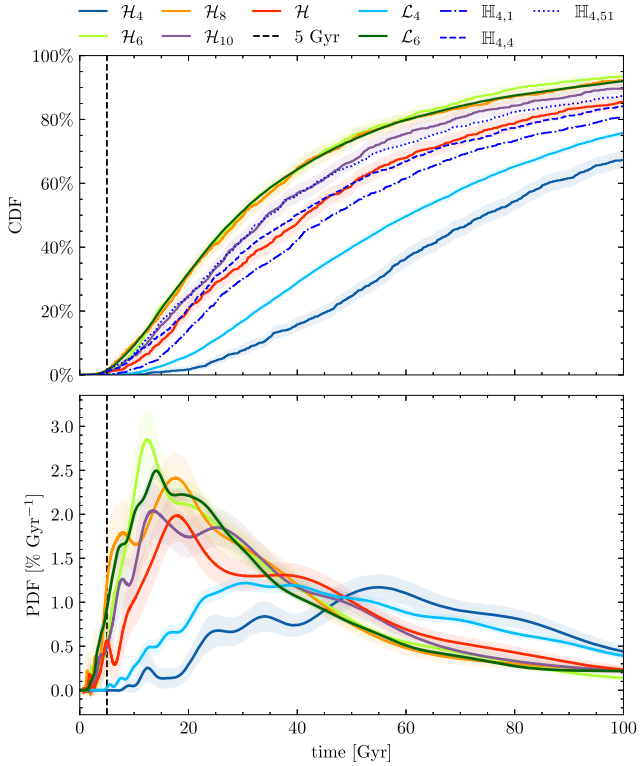

Figure 5. CDF and PDF of the first hitting time of Mercury's eccentricity at 0.7 over 100 Gyr with 90 per cent piecewise confidence interval, for the dynamical models $\mathcal{H}_{2n}$, $\mathbb{H}_{4,m}$, $\mathcal{L}_{2n}$, and $\mathcal{H}$. $\mathcal{H}$ denotes the 1042 orbital solutions of Gauss' dynamics in ML21.

the medians may suggest a convergence toward the value of 40 Gyr of Gauss' dynamics. On the other hand, the difference between $\mathcal{H}_4$ and the other truncated forced dynamics is still considerable. The median time for $\mathcal{H}_4$ is 75 Gyr, roughly doubling the value of $\mathcal{H}_6$. If we assume that the PDFs follow a Levy distribution $\rho(\tau) = (T_0/\pi\tau^3)^{1/2}E^{-T_0/\tau}$ over short times (ML21), with T_0 proportional to the median of the distribution, one easily understands how a difference by a factor of two in the medians of the PDFs results in very different probabilities over 5 Gyr. Indeed, the fact that the destabilization over 5 Gyr is a rare event greatly amplifies the disparity between $\mathcal{H}_4$ and the models of higher degree.

There is practically no difference between the statistics of $\mathcal{H}_6$ and $\mathcal{L}_6$ over this time-scale, which confirms the secondary effect of the second order in masses for the forced ISS and the statistics of the high Mercury eccentricities in particular. However, this effect is magnified for $\mathcal{H}_4$, the CDF of $\mathcal{L}_4$ approaching halfway the curves of higher degrees, with a median time of around 60 Gyr. Fig. 5 also shows the CDFs of $\mathbb{H}_{4,m}$, highlighting the impact of the leading harmonics at degree 6. With only the integrable term $\widetilde{\mathbb{H}}^{\mathbf{0},\mathbf{0}}_{(6)}$ considered, the CDF of $\mathbb{H}_{4,1}$ is already close to that of $\mathcal{H}$. When additional harmonics are added, their CDFs approach the curve of $\mathcal{H}_6$, as shown by $\mathbb{H}_{4,4}$ and $\mathbb{H}_{4,51}$.

5 DISCUSSION

Our findings suggest a remarkable analogy between the secular ISS and the Fermi–Pasta–Ulam–Tsingou (FPUT) problem, which consists in a chain of coupled weakly-anharmonic oscillators (Fermi et al. 1955). This is basically the same kind of interactions as in the secular planetary problem. Differently from Fermi's expectations, the

proper modes of oscillation of the FPUT dynamics remain far from the equipartition invoked in equilibrium statistical mechanics for a very long time. This has been related to the closeness of the FPUT problem to the integrable Toda dynamics, which does not allow any thermalization of its action variables (Flaschka 1974; Hénon 1974; Ferguson, Flaschka & McLaughlin 1982; Benettin, Christodoulidi & Ponno 2013). Although not integrable, and indeed chaotic, the Hamiltonian $\mathcal{H}_4$ plays a role similar to the Toda Hamiltonian, as it does not allow essentially any dynamical instability over 5 Gyr. The main question at this point is why the dynamics of $\mathcal{H}_4$ is practically stable over 5 Gyr. Once this is assessed, the small 1 per cent probability of an instability of the ISS may be conceived as a natural perturbative effect of terms of degree 6 and higher.

ACKNOWLEDGEMENTS

The authors are indebted to M. Gastineau for his support with TRIP. NHH is supported by a PhD scholarship of the Capital Fund Management (CFM) Foundation for Research. FM is supported by a grant of the French Agence Nationale de la Recherche (AstroMeso ANR-19-CE31-0002-01) and has been supported by a Paris Sciences & Lettres (PSL) post-doctoral fellowship. This project has been supported by the European Research Council (ERC) under the European Union's Horizon 2020 research and innovation programme (Advanced Grant AstroGeo-885250). This work was granted access to the HPC resources of MesoPSL financed by the Region Île-de-France and the project Equip@Meso (reference ANR-10-EQPX-29-01) of the programme Investissements d'Avenir supervised by the Agence Nationale pour la Recherche.

DATA AVAILABILITY

All data needed to evaluate the conclusions in this study are present in this paper and/or the Appendices.

REFERENCES

Abbot D. S., Webber R. J., Hadden S., Seligman D., Weare J., 2021, ApJ, 923, 236
Batygin K., Laughlin G., 2008, ApJ, 683, 1207
Batygin K., Morbidelli A., Holman M. J., 2015, ApJ, 799, 120
Benettin G., Christodoulidi H., Ponno A., 2013, J. Stat. Phys., 152, 195
Boué G., Laskar J., Farago F., 2012, A&A, 548, A43
Charpentier A., Flachaire E., 2015, L'Actualité économique, 91, 141
Cheng G., Chen Y.-C., 2019, Electron. J. Stat., 13, 2194
Cowling A., Hall P., 1996, J. R. Stat. Soc. B, 58, 551
Efron B., 1979, Ann. Stat., 7, 1
Ferguson W. E. J., Flaschka H., McLaughlin D. W., 1982, J. Comput. Phys., 45, 157
Fermi E., Pasta P., Ulam S., Tsingou M., 1955, Technical Report, Studies of Nonlinear Problems. Los Alamos National Laboratory
Flaschka H., 1974, Phys. Rev. B, 9, 1924
Gastineau M., Laskar J., 2011, ACM Communications in Computer Algebra, 44, 194
Gastineau M., Laskar J., 2021, TRIP Reference manual, TRIP 1.4.120. IMCCE, Paris Observatory
Gauss C., 1818, Werke, 3, 331
Hénon M., 1974, Phys. Rev. B, 9, 1921
Hoang N. H., Mogavero F., Laskar J., 2021, A&A, 654, A156
Laskar J., 1985, A&A, 144, 133
Laskar J., 1988, A&A, 198, 341
Laskar J., 1989, Nature, 338, 237
Laskar J., 1990, Icarus, 88, 266
Laskar J., 1994, A&A, 287, L9
Laskar J., 1997, A&A, 317, L75
Laskar J., 2005, Hamiltonian Systems and Fourier Analysis: New Prospects For Gravitational Dynamics. Cambridge Scientific Publishers Ltd, Cambridge
Laskar J., 2008, Icarus, 196, 1
Laskar J., Gastineau M., 2009, Nature, 459, 817(LG09)
Laskar J., Robutel P., 1995, Celest. Mech. Dyn. Astron., 62, 193
Laskar J., Simon J. L., 1988, Celest. Mech., 43, 37
Laskar J., Fienga A., Gastineau M., Manche H., 2011, A&A, 532, A89
Lithwick Y., Wu Y., 2011, ApJ, 739, 31
Mogavero F., Laskar J., 2021, A&A, 655, A1(ML21)
Mogavero F., Laskar J., 2022, A&A, 662, L3
Morbidelli A., 2002, Modern Celestial Mechanics: Aspects of Solar System Dynamics. Taylor & Francis, London and New York
Parzen E., 1962, Ann. Math. Stat., 33, 1065
Rosenblatt M., 1956, Ann. Math. Stat., 27, 832
Silverman B. W., 1986, Density Estimation for Statistics and Data Analysis. Chapman & Hall/CRC, London
Sussman G. J., Wisdom J., 1992, Science, 257, 56
Wilson E. B., 1927, J. Am. Stat. Assoc., 22, 209
Woillez E., Bouchet F., 2020, Phys. Rev. Lett., 125, 021101
Yang W., Zurbenko I., 2010, WIREs Comput. Stat., 2, 340

APPENDIX A: SECULAR DYNAMICS AT SECOND ORDER IN PLANETARY MASSES

We use the secular equations of motions of Laskar (1985, 1990, 2008, and references therein). They were obtained via series expansions in planetary masses, eccentricities, and inclinations, as well as through second-order analytical averaging over the rapidly changing mean longitudes of the planets. The expansion was truncated at the second order with respect to the masses and to degree 5 in eccentricities and inclinations. The equations include corrections from GR and Earth–Moon gravitational interaction. This leads to the following system of ordinary differential equations, denoted by $\mathcal{L}_6$ throughout this paper:

$$\frac{\mathrm{d}\omega}{\mathrm{d}t} = \sqrt{-1}\{\Gamma + \Phi_3(\omega, \bar{\omega}) + \Phi_5(\omega, \bar{\omega})\}, \tag{A1}$$

where $\omega = (z_1, \ldots, z_8, \zeta_1, \ldots, \zeta_8)$, with $z_k = e_k E^{j\varpi_k}$ and $\zeta_k = \sin(i_k/2)E^{j\Omega_k}$. The planets are indexed in order of increasing semi-major axis, as usual. The variable ϖ_k is the longitude of the perihelion, Ω_k is the longitude of the ascending node, e_k is the eccentricity, and i_k is the inclination. The function $\Phi_3(\omega, \bar{\omega})$ and $\Phi_5(\omega, \bar{\omega})$ are the terms of degree 3 and 5, respectively. The 16×16 matrix Γ is the linear Laplace–Lagrange system, which is slightly modified to make up for the higher order terms in the outer Solar system.

To mimic $\mathcal{H}_4$, we define the new model $\mathcal{L}_4$ by dropping the terms of degree 5 from the equations of the inner planets, that is:

$$\frac{\mathrm{d}\omega}{\mathrm{d}t} = \sqrt{-1}\{\Gamma + \Phi_3(\omega, \bar{\omega}) + \mathbb{D}\Phi_5(\omega, \bar{\omega})\}, \tag{A2}$$

where we introduced the diagonal matrix $\mathbb{D} = \mathrm{diag}(\mathbf{0}, \mathbf{1}, \mathbf{0}, \mathbf{1})$, with $\mathbf{0} = (0, 0, 0, 0)$ and $\mathbf{1} = (1, 1, 1, 1)$. It should be noted that the truncations behind the models $\mathcal{L}_6$ and $\mathcal{L}_4$ are defined with respect to the classical variables z_k, ζ_k, differently from the models $\mathcal{H}_{2n}$ that result from the expansion of $\mathcal{H}$ in the complex Poincaré variables $x_k \propto (1 - (1 - e_k^2)^{1/2})^{1/2} E^{j\varpi_k}$ and $y_k \propto (1 - e_k^2)^{1/4} \sin(i_k/2) E^{j\Omega_k}$.

We define ensembles of initial conditions by slightly varying a single variable of an inner planet at a time, while keeping other

Table A1. Offsets of the initial variables $k_i = e_i \cos \varpi_i$ and eccentricity e_i, with $i \in \{1, 2, 3, 4\}$ corresponding to the inner planets {Mercury, Venus, Earth, Mars}.

Variable	Offsets	ϵ	N	T (Gyr)
k_i	$-N\epsilon$ to $N\epsilon$	10^{-11}	5000	100
e_i	$-N\epsilon$ to $N\epsilon$	10^{-11}	10 000	5

Notes. Different initial conditions correspond to offsets of $n\epsilon$ in a single variable of a single planet for $n = -N, \ldots, N$, while other variables are kept to their nominal values. Each initial condition is used to compute a solution over the time interval $[0, T]$.

variables identical to their reference values, as shown in Table A1. For the integrations over 100 Gyr, we use the initial conditions varied from the variables $(k_i = e_i \cos \varpi_i)_{i=1,4}$ of the four inner planets, except for the solutions of $\mathcal{L}_4$, where only those varied from k_1 are used. For the solutions computed over 5 Gyr, the variables $(e_i)_{i=1,4}$ are varied to obtain the initial conditions. The solutions integrated up to 100 Gyr are included in the analysis of the statistics of the first 5 Gyr. Equations (A1) and (A2) are integrated from these ensembles of initial conditions to obtain the solutions of $\mathcal{L}_6$ and $\mathcal{L}_4$.

APPENDIX B: STATISTICS WITH DIFFERENT THRESHOLDS OF MERCURY'S ECCENTRICITY

We compute the CDFs of the first hitting time of Mercury's eccentricity at the three levels 0.7, 0.8, and 0.9, in order to test the dependency of the instability statistics on different thresholds. The results are shown in Fig. B1. Up to 5 Gyr, when the instability constitutes a rare event, the models of degree higher than 6 show consistency across high values of eccentricity. The difference between the CDFs of the three thresholds is relatively significant for the models at degree 6 ($\mathcal{H}_6$, $\mathcal{L}_6$), and even more so at degree 4 ($\mathcal{H}_4$, $\mathcal{L}_4$). For $\mathcal{H}_6$ and $\mathcal{L}_6$, only about half of the integrations exceeding 0.7 also goes beyond 0.9 in 5 Gyr. It should be noted that if Mercury's eccentricity goes beyond 0.9, it is likely that a catastrophic event will shortly ensue, whether it is a secular collision (ML21) or a numerical instability in the truncated dynamics. Therefore, the expected time that a solution of $\mathcal{H}_6$ spends in an unstable state of high Mercury eccentricity is longer, which makes $\mathcal{H}_6$ a prime model for the study of the unstable states of the ISS. Over a longer time-scale of 100 Gyr, when the destabilization is no longer a rare event, the difference of the CDFs with respect to the choice of the eccentricity threshold is small for the models at degree 4 and negligible for the rest.

APPENDIX C: DIFFERENCE BETWEEN PAST AND FUTURE FOR THE STATISTICS OF MERCURY'S ECCENTRICITY

In this work, we focus on the statistics of Mercury's eccentricity over long time-scales in the future. It is interesting to revert the time direction to obtain the statistics in the past for comparison. From the set of initial conditions defined according to Table A1, equations (A1) and (A2) are integrated in the direction of negative times to obtain 120 000 and 40 000 solutions spanning 5 and 100 Gyr, respectively, for both degrees 4 and 6.

The CDFs of the first hitting time of Mercury's eccentricity at 0.7 for $\mathcal{L}_4$ and $\mathcal{L}_6$ in two time directions are shown in Fig. C1. For both models, the difference between past and future is small but still noticeable initially, and gradually diminishes as time goes. The asymptotic convergence of the two time directions is physically expected, and has been also observed for the PDFs of the fundamental

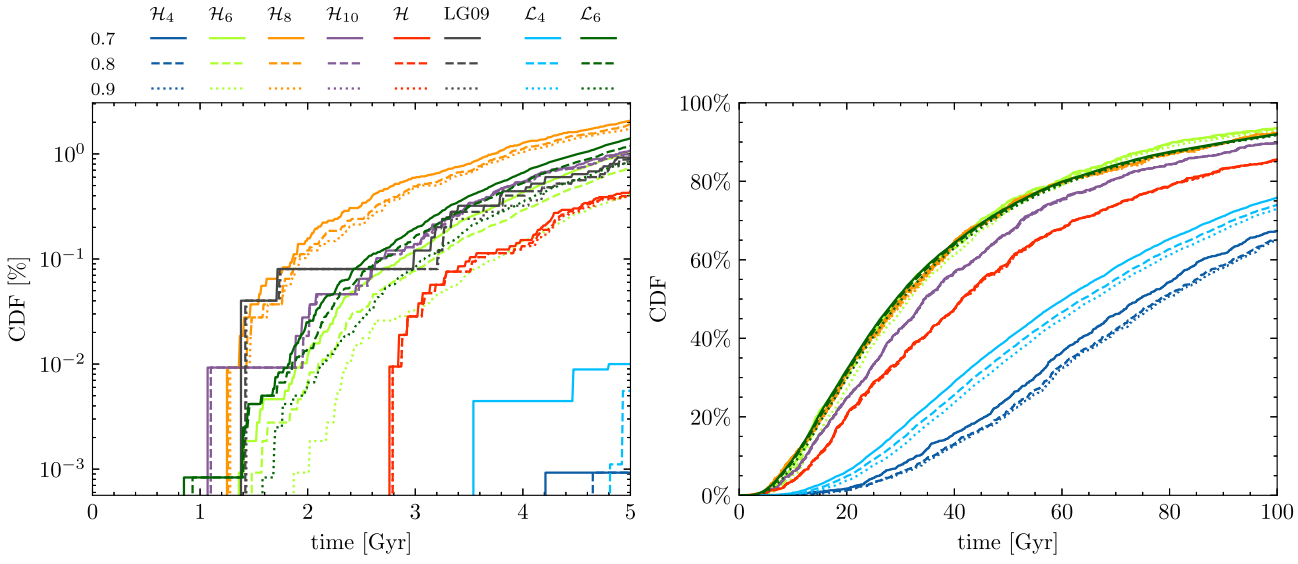

Figure B1. CDFs of the first hitting time of Mercury's eccentricity at the three thresholds 0.7, 0.8, and 0.9, up to 5 (left-hand panel) and 100 Gyr (right-hand panel) in the future for the dynamical models $\mathcal{H}_{2n}$, $\mathcal{H}$, $\mathcal{L}_{2n}$, and LG09. LG09 represents 2492 orbital solutions over 5 Gyr of LG09, while $\mathcal{H}$ denotes the 10 560 and 1042 solutions of Gauss' dynamics in ML21 spanning 5 and 100 Gyr, respectively. It should be noted that we use here the upper bound of estimation for $\mathcal{H}$, in which Mercury's eccentricity of a solution is assumed to exceed 0.9 after a secular collision, as explained in the main text.

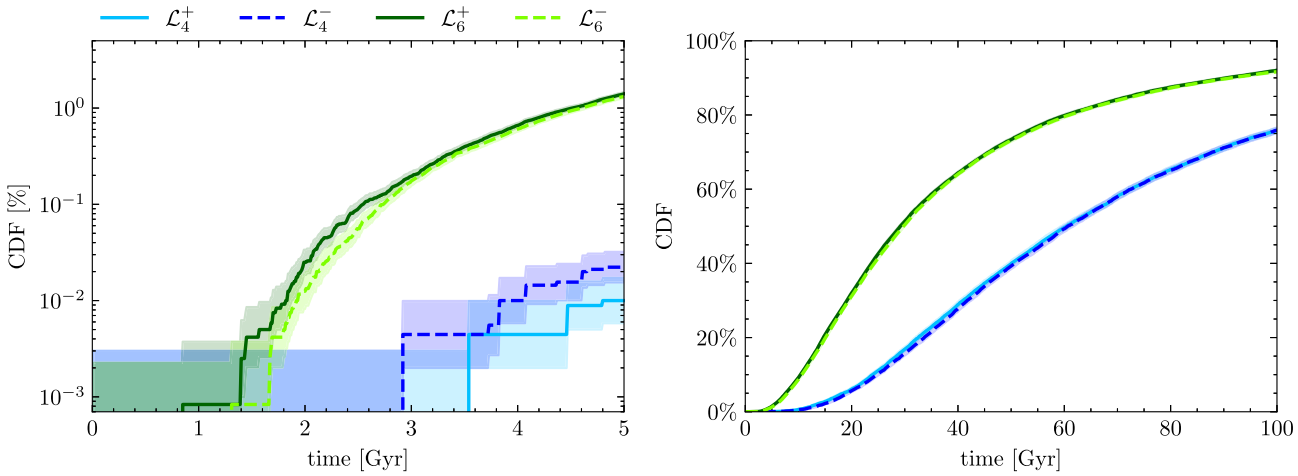

Figure C1. CDFs of the first hitting time of Mercury's eccentricity at 0.7 for the dynamical models $\mathcal{L}_{2n}$ over 5 Gyr (left-hand panel) and 100 Gyr (right-hand panel) in the two time directions, with 90 per cent confidence intervals. The integrations in the past are denoted by $\mathcal{L}_{2n}^-$, while $\mathcal{L}_{2n}^+$ denotes the integrations in the future.

frequencies of the Solar system (Hoang et al. 2021). Over the timescale of 100 Gyr, the CDFs of past and future are identical for both $\mathcal{L}_4$ and $\mathcal{L}_6$.

APPENDIX D: PDF ESTIMATION

In this section, we will briefly explain the methods to estimate the PDF of $\tau = \inf_t\{e_1(t) \geq 0.7\}$, that is, the first time that the eccentricity of Mercury e_1 reaches the threshold of 0.7 from our ensembles of integrations spanning from 0 to 100 Gyr.

Debiased KDE and bootstrap

KDE, also known as the Parzen–Rosenblatt window method, is a non-parametric estimator of the underlying PDF of a data set (Rosenblatt 1956; Parzen 1962). In this work, we use a bias-corrected version of the KDE to facilitate the uncertainty estimation by bootstrapping the data. We briefly present the method here (a detailed presentation can be found in Cheng & Chen 2019 and references therein). Let $\boldsymbol{X} = \{X_1, X_2, \ldots, X_n\}$ be a univariate independent and identically distributed (i.i.d.) sample drawn from an unknown probability density function $p(x)$. The KDE of the sample is then defined as

$$\widehat{p}_h(x|\boldsymbol{X}) = \frac{1}{nh}\sum_{i=1}^{n} K\left(\frac{x - X_i}{h}\right), \tag{D1}$$

where K is a non-negative kernel function and h is the bandwidth. In this work, we choose Silverman's (1986) rule of thumb for the selection of the optimal bandwidth and the standard Gaussian kernel. With this choice of bandwidth, the bias error and variance error of the KDE in equation (D1) are of the same order of magnitude. Therefore, the bootstrap method (Efron 1979), which measures the variance error by random resampling of the original data set, is not a consistent estimator of the total error of the KDE in equation (D1). One approach to this problem is to use a bias-corrected KDE, defined as

$$\widetilde{p}_h(x) = \widehat{p}_h(x) - \frac{h^2}{2}\sigma_K^2 \frac{d^2\widehat{p}_h(x)}{dx^2}, \tag{D2}$$

where $\sigma_K^2 = \int ||x||^2 K(x)dx$ is a constant depending on the kernel function K. With the debiased KDE in equation (D2), the bias error is reduced so that the total error is dominated by the variance error, which can be consistently estimated by the bootstrap method.

The procedure of the standard bootstrap (Efron 1979) is as follows. We resample the original data set $\boldsymbol{X}$ with replacement to obtain a bootstrap sample $\boldsymbol{X}^* = \{X_1^*, X_2^*, \ldots, X_n^*\}$. Equation (D2) is then applied to this bootstrap sample to obtain a bootstrap debiased KDE $\widetilde{p}_h^*(x|\boldsymbol{X}^*)$. We then repeat this procedure B times to obtain B bootstrap debiased KDEs $\widetilde{p}_h^{*(1)}, \cdots, \widetilde{p}_h^{*(B)}$. Because the distribution of $|\widetilde{p}_h^* - \widetilde{p}_h(x)|$ approximates that of $|\widetilde{p}_h - p(x)|$, from the sample of the B bootstrap KDEs, we can compute an asymptotically valid estimation of the piecewise confidence interval $\mathrm{CI}_{1-\alpha}(x)$, defined as

$$P(|\widetilde{p}_h - p(x)| < \mathrm{CI}_{1-\alpha}(x)) = 1 - \alpha. \tag{D3}$$

Boundary correction

Kernel density estimation of a PDF on a finite interval can be affected by non-negligible bias at the boundaries. In our work, the interval is defined by the total integration time, that is, [0, 100] Gyr in Fig. 5. The nature of the two boundaries is different, and they should be treated differently. At $t = 0$, the integrations start closely around a nominal value of $e_1 \approx 0.2$, therefore the PDF of the first hitting time of $e_1 = 0.7$ should be 0 when $t = 0$. This constraint suggests the log-transformation of the sample before applying the KDE (Charpentier & Flachaire 2015).

The boundary at 100 Gyr has no similar constraints, and we employ a pseudodata method to correct the bias (Cowling & Hall 1996). The idea is to use the original data set to generate fictitious data outside the interval of interest. Let $X_{(1)} < \ldots < X_{(n)}$ be the order statistics of the data $X_1, \ldots, X_n$ on the interval [0,1]. The extra data points generated in the range $(-\infty, 0)$ are defined by the three-point rule:

$$X_{(-i)} = -6X_{(i)} + 4X_{(2i)} - 3X_{(3i)}. \tag{D4}$$

To adapt the upper limit of the interval [0, 100] Gyr to this rule, we simply transform the data as $X_{(i)} \to (100 - X_{(i)})/100$. The pseudodata are then generated according to equation (D4), and the ensemble is back-transformed at the end. The number of pseudodata points is taken to be about 10 per cent of the sample size.

This paper has been typeset from a TEX/LATEX file prepared by the author.